One-pot preparation of magnetic nitrogen-doped porous carbon from lignin for efficient and selective adsorption of organic pollutants

Yuxin Tian（✉ 1227443679@qq.com）
　Shandong University of Science and Technology　https://orcid.org/0000-0002-6212-8961

Yanbo Yin
　Shandong University of Science and Technology

Zuoyu Jia
　Shandong University of Science and Technology

Hongming Lou
　South China University of Technology

Haifeng Zhou
　Shandong University of Science and Technology　https://orcid.org/0000-0003-2126-3988

Abstract

Efficient and rapid capture of organic pollutants from wastewater is an urgent problem to be solved by adsorbents. Nitrogen-doped magnetic porous carbon (M-PLAC) with three-dimensional porous structure was synthesized from lignin to adsorb MB and TC in wastewater. M-PLAC had high specific surface area (1252.21 m^2/g) and N element content (7.44%). The calculated equilibrium adsorption amount by M-PLAC for MB and TC was 645.52 and 1251.09 mg/g, respectively. The adsorption of MB and TC on M-PLAC conformed to the pseudo-second-order kinetic model, demonstrating that the adsorption process was attributed to chemisorption. The excellent adsorption performance was a synergistic effect among various adsorption mechanisms. The removal of MB and TC by M-PLAC showed fast and efficient characteristics, and exhibited high selectivity for TC in binary system. In addition, M-PLAC was suitable for a variety of complex water environments and had good regeneration performance, demonstrating potential advantages in practical wastewater treatment.

1. Introduction

Nowadays, the discharge of organic pollutants in wastewater has gradually become an environmental issue that has attracted much attention. Solving the pollution of water by organic dyes and antibiotics is one of the important challenges to be rose to urgently. Various important fields use organic dyes because of their color rendering properties such as cosmetics (Huang et al., 2015), papermaking (Katheresan et al., 2018) and leather (Zhao et al., 2011). Most organic dyes have complex aromatic structures and are refractory, carcinogenic, and mutagenic (Moussavi et al., 2016; Wang et al., 2016). Methylene blue (MB), as a common cationic dye, is widely applied in industrial and food production. Long-term exposure to MB-rich waste fluid will not only harm aquatic plants and organisms (Tan et al., 2015), but also cause serious damage to the human body, such as causing vomiting, allergic reactions and damage to the kidneys and liver (Jiao et al., 2022; Kundu et al., 2018). Similarly, antibiotics have attracted extensive concern in recent years because of their detection in surface water and food chain (Liu et al., 2017). Among them, tetracycline (TC) is extensively applied to animal husbandry and aquaculture. Nevertheless, most TC is difficult to metabolize through digestive systems of living organisms and can only be excreted in urine and feces, thus TC is released into the aquatic system in its original form (Leong et al., 2016). The TC released into the water environment will not only harm human health and ecological balance, but also cause drug resistance of micro-organisms (Yu et al., 2017). Therefore, how to efficiently and quickly remove organic pollutants in water environment has become the key of water pollution research.

At present, several methods including adsorption (Zhang et al., 2022), membrane separation (Zhang et al., 2019), photocatalytic degradation (Wu et al., 2022), biodegradation (Xiong et al., 2017) and redox (Kueasook et al., 2020) have been fully developed to treat wastewater rich in organic pollutants. Among them, adsorption method is regarded as an attractive approach to remove organic pollutants from wastewater because of its advantages of low energy consumption, simple operation, environmental friendliness and no secondary pollution (Tian and Zhou, 2022). Various materials have been developed to adsorb organic pollutants, such as graphene oxide (Salas et al., 2010), metal-organic frameworks (Wang

et al., 2018), zeolite (Seredych and Bandosz, 2007) and carbon nanotubes (Cheng et al., 2019). However, these materials still face problems such as cumbersome preparation process, poor selectivity, insufficient adsorption capacity and secondary pollution (Chen et al., 2017). Compared with these adsorbents, porous carbon is regarded as the most effective adsorbent to remove organic pollutants due to its relatively low investment, high modifiability, huge surface area and abundant porous structure (Kundu et al., 2018). For example, Kueasook et al. (2020) prepared multi-layered porous carbon from bagasse with a maximum MB adsorption amount of 100 mg/g. Zhao C. et al. (2020) published an environmentally friendly preparation of reed bioporous carbon by doping sludge for TC removal in aqueous solution ($q_{e\,max}$ = 153.4 mg/g).

Lignin, as a special class of renewable polyhydroxyl aromatic polymers, is widely present in plant cell walls (Bz et al., 2020). The abundant oxygen-containing groups in lignin, such as hydroxyl, methoxy, carbonyl, etc., show broad application prospects in terms of designability, adsorption performance, dispersibility and affinity for organic pollutants (Cedap et al., 2020; Zhao et al., 2021). Nevertheless, almost all lignin has been burnt as fuel, which not only wastes resources, but also leads to a large number of greenhouse gas emissions (Ponomarev and Sillanpää, 2019). Therefore, it is a promising alternative to make better use of lignin resources and convert them into lignin-based high-efficiency adsorbents. For instance, Brazil et al. (2020) prepared activated carbon possessed large specific surface area by microwave pyrolysis of sulfate lignin, which has good adsorption performance for MB in aqueous solution.

Although lignin-based activated carbon has improved the dye adsorption capacity to a high level, the simultaneous adsorption of two organic pollutants (TC and MB) by lignin-based activated carbon is rarely reported. Therefore, it is urgent to design a lignin-based activated carbon to remove different organic pollutants. At present, most studies only pay attention to the large adsorption amount of adsorbent, but often ignore the key characteristic of adsorption rate. At the same time, nitrogen doping can endow the activated carbon surface with unique electronic properties and abundant functional groups, thereby accelerating the adsorption efficiency. Herein, we successfully prepared a lignin-based nitrogen-doped magnetic porous carbon via facile one-pot method, which is expected to achieve rapid and efficient removal of MB and TC in wastewater within a wide pH range. The structural characterizations of porous carbon were investigated by SEM, N_2 physical adsorption, XRD, FT-IR and TG. The impacts of initial pH of the solution, pollutant concentration, adsorption time, system temperature and water quality were systematically studied. Ultimately, the removal mechanism was obtained through the adsorption kinetics, isotherm and thermodynamics research.

2. Materials And Methods

2.1. Materials

The purified lignin (PL) was procured from black liquor by sulfuric acid precipitation method (Tian and Zhou, 2022). Ferric nitrate and urea were purchased from Kelong Chemical Co., Ltd. (Chengdu, China).

Methylene blue (MB, $C_{16}H_{18}N_3SCl$) and tetracycline (TC, $C_{22}H_{24}N_2O_8$) were obtained from Macklin Reagent Co., Ltd. (Shanghai, China).

2.2. Preparation of M-PLAC

The process of preparing M-PLAC by one-pot method was as follows (Scheme 1): 2 g PL was mixed with 50 mL of 0.3 M ferric nitrate solution and then equal mass of urea and potassium hydroxide were sequentially added to the mixed solution. After stirring for 2 h in natural environment, the mixed solution was put into an oven at 105°C to evaporate the water, and the nitrogen-doped magnetic precursor was obtained. The pyrolysis process was carried out in a tube furnace. Under the conditions of nitrogen atmosphere (50 mL/min) and continuous temperature rise (10°C/min), the precursor was calcined to 800°C and maintained for 1 h. After washing and drying, the nitrogen-doped magnetic product (M-PLAC) was successfully prepared. For comparison, M@PL-AC was prepared by nitrogen doping and then activation at the same pyrolysis conditions.

2.3. Characterization

The surface microstructure and energy dispersive spectroscopy (EDS) of M-PLAC were detected by scanning electron microscopy (SEM, Apreo, FEI, Hillsboro, USA). Micromeritics ASAP 2020 system was applied to investigated the N_2 adsorption and desorption isotherms of M-PLAC at 77 K. The S_{BET} and pore distribution of M-PLAC was calculated by BET method and DFT equation, respectively. The inorganic crystal forms were determined using XRD (Riaku Utima IV) in the range of 5° to 85°. The Fourier-transform infrared spectroscopy (FT-IR, Nicolet 380) was applied to investigate the functional groups of samples. Thermogravimetric (TG) curve of M-PLAC was analyzed via thermal analyzer system (Mettler TGA 2, Swiss), which was scanned from 30°C to 1000°C at 10°C/min under N_2 atmosphere (100 mL/min).

2.4. Adsorption experiments

In a constant temperature shaker, 0.03 g of M-PLAC was added to 50 mL different concentrations of MB (from 300 to 600 mg/L) or TC (from 300 to 700 mg/L) solution at 35°C and 150 rpm. At different intervals, 1 mL of the mixed suspension was taken out for measurement. All tests were made in duplicate and the results were averaged.

Moreover, the impacts of various parameters including solution pH, system temperature and adsorption time on MB and TC adsorption were studied. The concentration of MB and TC was measured by UV-Vis spectrophotometer at 665 nm and 356 nm, respectively. Adsorption amount (q_e, mg/g) and removal rate (%) of MB and TC on M-PLAC were formulated as Eq. (1) and Eq. (2), respectively

$$q_e = \frac{C_0 - C_e}{m} \times V$$

1

$$Removal\,rate(\%) = \frac{C_0 - C_e}{C_e} \times 100$$

2

in which C_0 and C_e (mg/L) represents the original and ultimate concentration of organic pollutants, respectively, V (L) stands for the solution volume, and m (g) is the mass of M-PLAC.

2.5 Fast adsorption and selectivity adsorption

The fast adsorption experiment was conducted with low concentration of pollutants. The concentration of MB and TC solution was 50 and 100 mg/L, respectively. The selectivity adsorption experiment was conducted in a binary system of MB (50 mg/L) and TC (100 mg/L).

2.6 Effect of water quality

Deionized water, tap water, lake water and sea water were used to prepare 300 mg/L MB or TC solutions, and 0.03 g M-PLAC was evenly mixed in these solutions until adsorption equilibrium.

2.7 Regeneration and reusability of M-PLAC

Specifically, 0.03 g M-PLAC was mixed in 50 mL MB or TC solution (300 mg/L). After adsorption, M-PLAC covered with MB (or TC) was evenly dispersed in 0.1 M NaOH solution for separation, followed by washing with deionized water and anhydrous ethanol. The experiment went through five adsorption-desorption cycles, and the supernatant was measured in each cycle to obtain the q_e and removal rate.

3. Results And Discussions

3.1. Characterizations of M-PLAC

The microscopic morphology and morphological structure of M-PLAC are depicted in Fig. 1. M-PLAC is a rough porous block structure. Under the action of KOH, the pores on the surface of M-PLAC are developed and varied in size. Further magnifying the SEM image (Fig. 1b), there are some Fe_3O_4 particles distributed on M-PLAC surface, indicating that Fe_3O_4 have been successfully loaded. In addition, according to the SEM-EDS and mapping images, the elements such as O, Fe, and N, are evenly distributed on M-PLAC with the content of 11.10%, 16.34%, and 7.44%, respectively (Table S1), which also proves the successful introduction of Fe_3O_4 and N elements. The addition of nitrogen increases the negative charge density of M-PLAC, thus enhancing the interaction between the adsorbent and the pollutant cation, thus achieving excellent adsorption performance (Cao et al., 2016). Moreover, specific types of nitrogen functional groups on M-PLAC surface are also generally considered as adsorption sites (Chen et al., 2013; Yang et al., 2020). As a result, the unique morphology and surface characteristics of M-PLAC fully demonstrate its adsorption potential.

The porosity of M-PLAC was analyzed by the N_2 adsorption-desorption isotherm. As illustrated in Fig. 2a, the isotherm is typical type IV based on IUPAC classification (Cui et al., 2018). The adsorption capacity of N_2 rises promptly at low P/P_0, which proves the microporous properties of M-PLAC. Afterwards, the N_2 adsorption capacity rises slowly with increasing P/P_0, indicating that there are amounts of mesoporous in M-PLAC. In addition, there is an obvious H4 type hysteresis loop on the isotherm, representing the capillary condensation of N_2 in the mesopores (Yang et al., 2020). The hysteresis loop is closed at P/P_0 = 0.4, proving the existence of small mesopores in M-PLAC (Wang et al., 2020). The S_{BET} of M-PLAC is 1252.21 m^2/g calculated by BET method. According to the pore size distribution curve of M-PLAC, most of the pores are concentrated below 10 nm (Fig. 2b), which suggests that M-PLAC is mainly composed of mesopores and micropores. A weak peak appears in the range of about 100 nm, suggesting the presence of a small number of large pores in M-PLAC. The average pore size (D_p) of M-PLAC is only 2.99 nm, while the total pore volume (V_{tot}), the micropore volume (V_{mic}) and the external area volume (V_{ext}) are 0.9359, 0.4386 and 0.4977 cm^3/g, respectively. Ultra-high S_{BET} and rich pore structure increase the contact area between organic pollutants and M-PLAC and provide more adsorption sites for adsorption reactions (Zhang et al., 2020).

The XRD pattern of M-PLAC is illustrated in Fig. 2c. The derivative peaks at 2θ = 26.4° and 43.5° represent the (002) and (100) planes of amorphous carbon and crystalline carbon, respectively (Zhang et al., 2014), indicating the presence of amorphous carbon and graphitized structures in M-PLAC (Zhu et al., 2018). On the other hand, the five typical characteristic peaks at 35.4°, 43.1°, 53.5°, 57.0°, 62.6° correspond to (311), (400), (422), (551) and (440) crystal structures of Fe_3O_4, respectively (JCPDS NO. 89−0691) (Dai et al., 2021), which proves the successful loading of Fe_3O_4 nanoparticles.

The TG/DTG measurements in N_2 atmosphere were designed to assess the weight loss of M-PLAC over the temperature range of 300−1000°C. As displayed in Fig. 2d, there are roughly four stages in the weight loss curve of M-PLAC. The first occurrence of weight loss (14.76%) in the range of 30−160°C is attributed to the release of adsorbed water on the M-PLAC surface (Pan et al., 2017). With increasing temperature from 160 to 730°C, 15.50% of the weight loss may be caused by the elimination of unstable functional groups (Li et al., 2019). The 13.26% of weight loss in the third stage (730−830°C) is caused by the decomposition of more stable functional groups. In addition, the combustion of the carbon skeleton is the main cause of weight loss at higher temperature (Pan et al., 2017).

The FT-IR spectra of raw material PL and M-PLAC are recorded in Fig. 3. The characteristic peaks observed at 3430, 2933 and 2841 cm^{-1} in the PL are ascribed to the O-H and C-H stretching vibration, respectively (Shi et al., 2020; Zhao et al., 2021; Zhou et al., 2020). The bands centered in 1615 – 1415 cm^{-1} are attributed to aromatic ring vibrations, which are considered to be the most typical characteristic of PL infrared bands (Gao et al., 2013; Zhang et al., 2018). The peaks at 1325, 1115 and 828 cm^{-1} are the typical syringyl (S) peaks, while the band around 1212 cm^{-1} originates from phenolic hydroxyl groups and ethers (Tejado et al., 2007; Zhao, Y. et al., 2020). After KOH activation, some characteristic peaks

observed in PL could still be observed in M-PLAC, such as 3430, 1615 and 1115 cm^{-1}. The most significant change is the disappearance or weakening of the functional groups, which may be caused by the KOH erosion and decomposition of lignin. The weakening of hydroxyl peak (3430 cm^{-1}) indicates that irregular amorphous carbon structure may be formed.

3.2. Adsorption performance

3.2.1 Effect of pollutant concentration and adsorption time

Experimental parameters, including pollutant concentration, adsorption time and system temperature, are closely related to the adsorption capacity. According to Fig. 4a and b, as MB concentration increases from 300 to 500 mg/L, the adsorption amount at equilibrium on M-PLAC enhances from 433.86 to 534.03 mg/g. Similarly, the equilibrium adsorption amount of TC also increases with increasing TC concentration. Visibly, the mass transfer driving force generated by the concentration gradient is in favor of overcoming the resistance of pollutant molecules from the solution to M-PLAC surface, and ultimately promote the adsorption reaction (Dai et al., 2021). In addition, the adsorption equilibrium time of different organic pollutants is different. For MB, the adsorption process can be divided into two stages. At the initial contact stage, a lot of holes and active sites on M-PLAC surface are rapidly occupied by MB molecules (Yao et al., 2020). The adsorption process rapidly reaches the equilibrium stage, which reflects the potential of M-PLAC to rapidly adsorb MB. By comparison, the adsorption process of TC molecule on M-PLAC is relatively mild. There are three stages in the adsorption process of TC. The first stage is the fast adsorption stage. A linear increase of TC adsorption amount can be observed at this stage (0–4 h). The second stage is the slow adsorption stage. With the decrease of effective adsorption vacancies of M-PLAC, the adsorption capacity of TC increases slowly until the adsorption equilibrium.

3.2.2 System temperature

Figure 4c and d describe the effect of temperature on MB and TC adsorption by M-PLAC. The raising of temperature contributes to the improvement of adsorption performance. The rising temperature may increase the confusion degree of pollutant molecules, which increases the collision probability of pollutant and M-PLAC, thus further promoting the binding of pollutant molecules to the surface active sites of adsorbents. Furthermore, the increase amplitude of adsorption amount decreases as the temperature rises. When the temperature increases from 45 to 55°C, the adsorption capacities of MB and TC increase only 0.40% and 2.17% respectively, which may be due to the saturation of M-PLAC surface active sites.

3.2.3 Effect of initial pH

The initial pH value is a key factor e to determine the adsorption behavior. It not only affects the charge of functional groups on adsorbents, but also controls the structure and morphology of target adsorbates (Liu et al., 2014). As displayed in Fig. 5a, the pH value of zero charge (pH$_{PZC}$) of M-PLAC is 7.30. When

the solution pH is lower than 7.30, M-PLAC is in a positive charge state due to protonation and gradually deprotonated to a negative charge state as pH increases (Jang et al., 2018). TC is a complex amphoteric organic compound, which exists in four forms at different pH values: H_4TC^+ with positive charge (pH < 3.3), amphoteric ion H_3TC (3.4 < pH < 7.6), and negative charge H_2TC^- (7.6 < pH < 9.7) and HTC^{2-} (pH > 9.7) (Zhu et al., 2014a). By contrast, the structure of MB molecules in solution is relatively stable.

According to Fig. 5b, the adsorption amount of MB on M-PLAC is little affected by the initial solution pH. In the pH range of 2−10, the adsorption amount of MB increases slightly from 415.23 to 462.52 mg/g. Under acidic conditions, the protonated binding sites (-OH and -COOH) on M-PLAC surface are positively charged. The interaction between MB^+ and positively charged M-PLAC is limited by competitive adsorption and electrostatic repulsion (Yu et al., 2017). As solution pH rises, the electrostatic attraction between M-PLAC with weakened protonation on the surface and MB^+ becomes stronger, thus promoting the adsorption. Nevertheless, the adsorption amount of MB is not significantly enhanced, indicating that other mechanisms take part in the adsorption process in addition to electrostatic interaction. In particular, π-π stacking interaction between aromatic rings in M-PLAC and MB also plays a vital role in the adsorption (Fu et al., 2016). Moreover, the TC adsorption on M-PLAC also shows similar results. When pH value increases from 2 to 10, the adsorption amount of M-PLAC for TC increases from 589.91 to 662.41 mg/g. It is worth noting that when pH is 8−10, a large amount of TC can be adsorbed despite the strong electrostatic repulsion between M-PLAC with negative surface charge and negative ions H_2TC^- and HTC^{2-}, indicating that electrostatic attraction is not the main controlling effect of adsorption. The adsorption of TC by M-PLAC is driven by multiple mechanisms including electrostatic interaction, pore-filling effect and π-π electron-donor-receptor (EDA) (Tian and Zhou, 2022; Zhu et al., 2014b). The results show that M-PLAC exhibits excellent adsorption performance for MB and TC in the wide pH range, which further proves its great potential in practical wastewater treatment.

3.2.4 Adsorption kinetics

Pseudo-first-order (PFO) and pseudo-second-order (PSO) kinetic models were applied to evaluate the possible rate control steps during the adsorption process. The kinetic equations are shown in Eq. (3) and Eq. (4), the fitted curves and detailed data are shown in Fig. S2 and Table 1.

$$ln(q_e - q_t) = lnq_e - k_1t$$

3

$$\frac{t}{q_t} = \frac{t}{q_e} + \frac{1}{k_2q_e^2}$$

4

In which q_e and q_t (mg/g) means the adsorption capacity at equilibrium and time t, respectively; k_1 (min^{-1}) and k_2 (mg/g·min) represent the rate constants of PFO and PSO.

At three concentrations of MB, the R^2 values of PSO (0.9835–0.9999) are much higher than those of PFO (0.7692–0.8433), indicating that chemisorption is the rate-control step in the adsorption process of MB. For TC, the R^2 values of PSO are similar to those of the PFO. However, the theoretical q_e calculated by PSO is more consistent with the actual $q_{e(exp)}$. As an example, at 700 mg/L, the q_e value calculated by PSO is 699.30 mg/g, while $q_{e(exp)}$ is 706.76 mg/g. It suggests that the adsorption of TC is mainly controlled by chemisorption, and physical effects such as pore-filling also play a vital role in the adsorption process.

To investigate the controlling factors of adsorption diffusion, the particle internal diffusion model was applied to fit the adsorption data of MB and TC. The model mathematical representation is shown in Eq. (5).

$$q_t = K_{id}t^{0.5} + C$$

5

In which q_t (mg/g) denotes the adsorption amount at time t; K_{id} (mg/g min$^{0.5}$) means the internal diffusion rate constant; C means the internal diffusion model constant.

As illustrated in Fig. S2c, the fitting plot of MB can be divided into two linear ranges, demonstrating two stages in MB adsorption. The first stage is attributed to the transport of MB molecules from solution to the outer surface of M-PLAC, which is controlled by molecular diffusion and membrane diffusion (Yu et al., 2021). The second stage may be the further diffusion of MB molecules in the pores of M-PLAC, which is a gradual internal diffusion of particles (Zeng et al., 2021). Compared with MB, the fitting diagram of TC can be divided into three linear ranges: (I) The first stage is the transfer of TC molecules from the solution to the outer surface of M-PLAC. Due to the highest initial concentration, TC molecules rapidly diffuse from the solution to the outer surface of the adsorbent under the action of high mass transfer power. (II) In the second stage, TC molecules diffuse to the inner surface of the M-PLAC while occupying the adsorption sites on the outer surface of M-PLAC(Chen et al., 2020). (III) The final stage is the adsorption of TC on the inner surface of M-PLAC holes. At this stage, the residual TC concentration in the solution is low, and the adsorption rate decreases. The adsorption process gradually approaches equilibrium. In addition, the diffusion rate constants of these stages are in the order of $K_{i,1} > K_{i,2} > K_{i,3}$ (Table 2), indicating that boundary layer thickness gradually thickens and boundary effect resistance gradually increases (Yu et al., 2017). The internal diffusion models of MB and TC do not pass through the origin ($C \neq 0$), reflecting that internal diffusion is only one of the steps to control the adsorption. The control process of adsorption rate is the result of the interaction of multiple kinetic models (Zhang et al., 2021).

Table 1
Fitting parameters of adsorption kinetic models of MB and TC by M-PLAC.

	C_0 (mg/L)	$q_{e(exp)}$ (mg/g)	PFO k_1 (min^{-1})	q_e (mg/g)	R^2	PSO k_2 (g/mg/min)	q_e (mg/g)	R^2
MB	300	433.80	0.0133	19.12	0.8322	0.00368	432.90	0.9999
	400	502.43	0.0917	27.57	0.8433	0.00350	442.48	0.9835
	500	534.03	0.0895	32.38	0.7692	0.00225	529.10	0.9999
TC	400	596.29	0.0875	193.01	0.9906	0.00169	591.72	0.9977
	500	680.75	0.0772	266.86	0.9755	0.00150	666.67	0.9942
	700	706.76	0.0858	298.77	0.9891	0.00143	699.30	0.9945

Table 2
Parameters of internal diffusion model for MB and TC adsorption by M-PLAC.

Parameters		Initial concentration of MB (mg/L) 300	400	500	Initial concentration of TC (mg/L) 400	500	700
I	$K_{i,1}$ (mg/g min$^{0.5}$)	13.20	6.82	12.78	66.90	74.13	63.85
	C_1 (mg/g)	366.38	477.84	451.58	357.64	376.66	384.34
	R^2	0.9130	0.9592	0.9605	0.9968	0.9879	0.8456
II	$K_{i,2}$ (mg/g min$^{0.5}$)	-			30.57	37.63	52.86
	C_2 (mg/g)	-			414.82	422.27	386.20
	R^2	-			0.9999	0.9997	0.9114
III	$K_{i,3}$ (mg/g min$^{0.5}$)	0.56	0.99	1.11	13.30	25.90	21.53
	C_3 (mg/g)	422.47	482.22	511.11	505.85	505.02	560.49
	R^2	0.9131	0.9398	0.9302	0.9610	0.9521	0.9576

3.2.5 Adsorption isotherm

Two adsorption isotherm models, Langmuir and Freundlich models were applied to investigate the relationship between the adsorbate and the adsorbent (M-PLAC). The data were fitted using Eq. (6) and Eq. (7).

$$q_e = \frac{q_m K_L C_e}{1 + K_L C_e}$$

6

$$q_e = K_F C_e^{1/n}$$

7

where q_e (mg/g) and C_e (mg/L) defines as the adsorption amount at equilibrium and the equilibrium concentration of MB and TC, respectively; q_m (mg/g) means the theoretical saturated adsorption amount, and K_L (L/mg), K_F and $1/n$ denote the Langmuir and Freundlich constants, respectively.

Adsorption isotherm can not only easily judge the nature of adsorption, but also obtain the maximum adsorption amount under the best conditions. As illustrated in Fig. 6 and Table 3, the R^2 of Langmuir model for MB and TC are higher than those of Freundlich model. This result demonstrates that the Langmuir model is more suitable for the adsorption process. The adsorption of MB and TC on M-PLAC is homogeneous and monolayer process. At 55°C, the maximum adsorption amount of MB and TC on M-PLAC calculated by Langmuir model is 645.52 and 1251.09 mg/g, respectively, suggesting that M-PLAC exhibits excellent adsorption effect for MB and TC.

Table 3
Fitting parameters of adsorption isotherms of MB and TC by M-PLAC.

	T (°C)	Langmuir			Freundlich		
		K_L (L/mg)	q_m (mg/g)	Adj-R^2	K_F (L/g)	$1/n$	Adj-R^2
MB	25	0.0098	541.08	0.9935	268.78	0.1243	0.8670
	35	0.0245	550.57	0.9816	307.29	0.1051	0.8554
	45	0.0338	570.98	0.9806	331.67	0.0992	0.8179
	55	0.5500	645.52	0.9651	359.19	0.0875	0.9448
TC	25	0.2752	631.15	0.9815	283.39	0.2075	0.9484
	35	0.1428	768.01	0.9122	330.52	0.1415	0.8435
	45	0.0336	875.72	0.9680	332.18	0.0822	0.8932
	55	0.1642	1251.09	0.9600	367.52	0.1908	0.9527

3.2.6 Thermodynamic analysis

To further investigate the adsorption process and possible adsorption mechanism of MB and TC by M-PLAC, the thermodynamic analysis was carried out. Thermodynamic parameters (such as Gibbs free energy change (ΔG (kJ/mol)), enthalpy change (ΔH (kJ/mol)) and entropy change (ΔS (J/mol/K)) at different temperatures are calculated as follows:

$$\ln K_d = -\frac{\Delta H}{RT} + \frac{\Delta S}{R}$$

8

$$\Delta G = \Delta H - T\Delta S$$

9

$$K_d = \frac{C_0 - C_e}{C_e} \times \frac{V}{m}$$

10

in which K_d (mL/g) is the equilibrium constant, R represents the gas constant 8.314 (J/mol/K), T (K) is the absolute temperature. As depicted in Fig. 7, we can get the ΔH and ΔS from the slope and intercept of the straight line.

As illustrated in Fig. 7, the adsorption capacity of M-PLAC for MB and TC increases with increasing temperature, reflecting an endothermic adsorption process. The thermodynamic parameters calculated by fitting are exhibited in Table 3. The ΔG values at all temperatures are negative, showing that the adsorption process is spontaneous. In addition, ΔG value decreases with increasing temperature, indicating that higher temperature can provide stronger driving force, which is favorable for adsorption. The positive ΔH reveals an endothermic process. The positive ΔS demonstrates the affinity of M-PLAC for MB and TC and the increased disorder of solid/liquid interface (Shi et al., 2020). In addition, according to previous studies (Hu et al., 2020), the adsorption of contaminant molecules on M-PLAC reduces their disorder degree, while the disorder degree of water molecules on M-PLAC increases significantly, which further results in an enhancement in the system entropy. Therefore, the increase of ΔS is the main driving force of adsorption process (Yu et al., 2017).

Table 4
The adsorption thermodynamic parameters of MB and TC adsorption on M-PLAC at various temperatures.

Adsorbates	T (K)	ΔG (kJ/mol)	ΔH (kJ/mol)	ΔS (J/mol/K)
MB	298	-19.72	4.71	82.00
	308	-20.54		
	318	-21.36		
	328	-22.18		
TC	298	-21.19	20.19	138.84
	308	-22.58		
	318	-23.96		
	328	-25.35		

3.3 Fast adsorption and selectivity adsorption of organic pollutants

In addition to pursuing higher adsorption amount, the adsorption speed of organic pollutants is also worth paying attention to. As depicted in Fig. 8a, the maximum absorbance of MB decreases remarkably with the extension of contact time. MB in the solution is completely adsorbed by M-PLAC after only 15 min, which fully highlights the characteristics of fast adsorption rate and high adsorption efficiency of MB by M-PLAC. In addition, from the optical image in Fig. 8a, the adsorption process of MB on M-PLAC can be clearly observed through the fading of MB solution. Similarly, TC can be removed by M-PLAC after 60 min (Fig. 8b). For investigating the adsorption characteristics of M-PLAC in complex system, the binary organic pollutant system was obtained by mixing MB and TC. As observed in Fig. 8d, all pollutants in the binary system are completely removed within 60 min. However, compared with the single solution, the adsorption rate of MB is reduced while TC hardly has any effect. Therefore, M-PLAC exhibits good selectivity to TC. The selectivity of M-PLAC to TC mainly depends on its abundant pore structure and surface characteristics. At the same time, the firm electrostatic interaction between the high-density of negatively charged groups (such as -COOH and -OH) existing on the surface of M-PLAC and MB$^+$ also promotes the efficient adsorption of MB by M-PLAC.

3.4 Effect of water quality

For investigating the adsorption performance of M-PLAC in actual water environment, the effect of water quality (such as deionized water, tap water, lake water and sea water) on the adsorption of organic pollutants was studied. Compared with the solution configured with deionized water, the influence of real environmental water quality on MB adsorption can be ignored (Fig. 9). In comparison, water quality has an obvious effect on TC adsorption. The adsorption efficiency of TC in tap water remains at 93.48%,

while it is 84.57% and 85.97% in lake water and sea water, respectively. This may be related to the fact that solid impurities occupy the adsorption site in the real water environment and the higher ion content reduces the interaction between TC molecules and M-PLAC (Xie et al., 2016). However, the adsorption amount of TC by M-PLAC in real water environment is still as high as 447.54 mg/g. The results prove that M-PLAC can adapt to various water qualities and can remove MB and TC efficiently and conveniently.

3.5 Reusability of M-PLAC

The reusability of adsorbent is always a relatively important index to evaluate its adsorption performance in practical application. The regeneration and reusability of M-PLAC for MB and TC removal were systematically investigated. As displayed in Fig. 13, the adsorption amount of MB is 369.06 mg/g after 5 cycles, which only drops to 85.22% of the original adsorption amount. In contrast, during TC adsorption, the larger decrease of adsorption amount originates from the irreversible losing of adsorption sites on M-PLAC surface. After 5 cycles, the adsorption amount of TC is still up to 222.51 mg/g, which maintains 51.38% of the original adsorption capacity. The results demonstrate that M-PLAC has excellent reuse performance and can be applied to treat wastewater containing MB and TC. At the same time, the magnetic separation characteristic of M-PLAC was evaluated by measuring its magnetic hysteresis curve. As illustrated in Fig. 10b, the saturation magnetization of M-PLAC is 26.02 emu/g. After adsorption, M-PLAC can be readily recovered from wastewater under the action of external magnetic field (inset of Fig. 10b), which further simplifies the solid-liquid separation process and facilitates the recovery and reuse of M-PLAC. In addition, the correlations of adsorption-desorption cycle are investigated in Fig. 10c and d. The R^2 of MB and TC is 0.9536 and 0.9864, respectively, indicating that the removal rate of MB and TC on M-PLAC is negatively correlated with the cycle index.

3.6 Adsorption mechanism of MB and TC on M-PLAC

FT-IR was applied to explore the functional group changes of M-PLAC after adsorption. As illustrated in Fig. 3, after the adsorption of MB and TC, two new characteristic peaks appear at 1312 cm^{-1} and 1464 cm^{-1}, representing the tensile vibration of C-N and -NH_2 of MB and TC molecules (Gautam and Hooda, 2020; Zhang et al., 2014), respectively, indicating that MB and TC molecules have been captured on the surface of M-PLAC. On the other hand, some slight changes are observed in the functional groups of M-PLAC after adsorption, indicating that functional groups play a vital role in the adsorption process. Combined with the results of kinetic study, the adsorption process of both MB and TC on M-PLAC is mainly chemisorption. At the same time, hydrogen bonding and the π-π stacking between MB and M-PLAC also promote the adsorption process. The TC adsorption by M-PLAC is attributed to various adsorption mechanisms, including electrostatic interaction, hydrogen bonding, hole filling effect and π-π EDA interaction (Scheme 2).

4. Conclusion

In the present work, a functional magnetic nitrogen-doped porous carbon (M-PLAC) was successfully synthesized via one-pot simple carbonization and activation using lignin as raw material and urea as nitrogen source to remove organic pollutants MB and TC. M-PLAC had large S_{BET} (1252.21 m^2/g) and abundant pore structure (V_{tot} = 0.9359 cm^3/g). M-PLAC could effectively remove MB and TC over a wide pH range. The adsorption processes of MB and TC on M-PLAC were in accordance with PSO and Langmuir model. The results showed that the adsorption behaviors of MB and TC by M-PLAC were chemical adsorption and monolayer adsorption. At 55°C, the maximum adsorption amount of M-PLAC for MB and TC was 645.52 and 1251.09 mg/g, respectively. In terms of thermodynamics, the adsorption of MB and TC was endothermic and spontaneous. Interestingly, M-PLAC could not only efficiently and quickly remove cation MB and TC in aqueous solution, but also adapted to a variety of complex water environments, reflecting the great potential of M-PLAC in practical application. Meanwhile, M-PLAC had good reusability and was easily separated by external magnetic field due to the presence of Fe_3O_4 magnetic particles. In conclusion, M-PLAC is a kind of functionalized activated carbon that is simple to prepare, efficient, fast and easy to separate, showing excellent adsorption potential in the treatment of organic pollutants in complex practical wastewater.

Declarations

- Ethics approval and consent to participate

Not applicable.

- Consent for publication

Not applicable.

- Availability of data and materials

Not applicable.

- Competing interests

The authors declare that they have no competing interests.

- Funding

- Authors' contributions

References

1. Brazil T, Gonçalves M, Junior M, Rezende M (2020) A statistical approach to optimize the activated carbon production from Kraft lignin based on conventional and microwave processes. Microporous and Mesoporous Mater 308:110485

2. Bz A, Dya B, Xqa C, Yong Q, Mya C, QI A (2020) Influences of aggregation behavior of lignin on the microstructure and adsorptive properties of lignin-derived porous carbons by potassium compound activation. J Ind Eng Chem 82(111):220–227

3. Cao Y, Huang J, Li Y, Qiu S, Liu J, Khasanov A, Khan M, Young D, Peng F, Cao D, Peng X, Hong K, Guo Z (2016) One-pot melamine derived nitrogen doped magnetic carbon nanoadsorbents with enhanced chromium removal. Carbon 109:640–649

4. Cedap A, Cdcn A, Dfdss B, Jado B, Esds A (2020) Organosolv lignin/Fe_3O_4 nanoparticles applied as a β-glucosidase immobilization support and adsorbent for textile dye removal. Ind Crops Prod 146:112167

5. Chen B, Cao Y, Zhao H, Long F, Feng X, Li J, Pan X (2020) A novel Fe(3+)-stabilized magnetic polydopamine composite for enhanced selective adsorption and separation of Methylene blue from complex wastewater. J Hazard Mater 392:122263

6. Chen C, Zhang J, Zhang B, Yu C, Peng F, Su D (2013) Revealing the enhanced catalytic activity of nitrogen-doped carbon nanotubes for oxidative dehydrogenation of propane. Chem Commun 49(74):8151–8153

7. Chen F, Gong A, Zhu M, Chen G, Lacey S, Jiang F, Li Y, Wang Y, Dai J, Yao Y (2017) Mesoporous, Three-Dimensional Wood Membrane Decorated with Nanoparticles for Highly Efficient Water Treatment. ACS Nano 11(4):4275

8. Cheng J, Gu J, Tao W, Wang P, Liu L, Wang C, Li Y, Feng X, Qiu G, Cao F (2019) Edible fungus slag derived nitrogen-doped hierarchical porous carbon as a high-performance adsorbent for rapid removal of organic pollutants from water. Bioresour Technol 294:122149

9. Cui Y, Wang H, Xu X, Lv Y, Liu W, Chen S, Wang X (2018) Nitrogen-doped porous carbons derived from a natural polysaccharide for multiple energy storage devices. Sustainable Energy Fuels 2:381–391

10. Dai K, Zhao G, Kou J, Wang Z, Zhang J, Wu J, Yang P, Li M, Tang C, Zhuang W, Ying H (2021) Magnetic mesoporous sodium citrate modified lignin for improved adsorption of calcium ions and methylene blue from aqueous solution. J Environ Chem Eng 9(2):105180

11. Fu J, Xin Q, Wu X, Chen Z, Yan Y, Liu S, Wang M, Xu Q (2016) Selective adsorption and separation of organic dyes from aqueous solution on polydopamine microspheres. J Colloid Interface Sci 461:292–304

12. Gao Y, Yue Q, Gao B, Sun Y, Wang W, Li Q, Wang Y (2013) Preparation of high surface area-activated carbon from lignin of papermaking black liquor by KOH activation for Ni(II) adsorption. Chem Eng J 217:345–353

13. Gautam D, Hooda S (2020) Magnetic Graphene Oxide/Chitin Nanocomposites for Efficient Adsorption of Methylene Blue and Crystal Violet from Aqueous Solutions. J Chem Eng Data 65(8):4052–4062

14. Hu L, Guang C, Liu Y, Su Z, Gong S, Yao Y, Wang Y (2020) Adsorption behavior of dyes from an aqueous solution onto composite magnetic lignin adsorbent. Chemosphere 246:125757

15. Huang B, Zhou X, Jing C, Wu G, Lu X (2015) Determination of malachite green in fish based on magnetic molecularly imprinted polymer extraction followed by electrochemiluminescence. Talanta 142:228–234

16. Jang H, Yoo S, Choi Y, Park S, Kan E (2018) Adsorption isotherm, kinetic modeling and mechanism of tetracycline on Pinus taeda-derived activated biochar. Bioresour Technol 259:24–31

17. Jiao T, Ren C, Lin S, Zhang L, Xu X, Zhang Y, Zhang W, Liang P (2022) The extraction mechanism research for the separation of indole through the formation of deep eutectic solvents with quaternary ammonium salts. J Mol Liq 347:118325

18. Katheresan V, Kansedo J, Lau S (2018) Efficiency of Various Recent Wastewater Dye Removal Methods: A Review. J Environ Chem Eng 6(4):4676–4697

19. Kueasook R, Rattanachueskul N, Chanlek N, Dechtrirat D, Watcharin W, Amornpitoksuk P, Chuenchom L (2020) Green and facile synthesis of hierarchically porous carbon monoliths via surface self-assembly on sugarcane bagasse scaffold: Influence of mesoporosity on efficiency of dye adsorption. Microporous and Mesoporous Mater 296:110005

20. Kundu S, Chowdhury I, Naskar M (2018) Hierarchical Porous Carbon Nanospheres for Efficient Removal of Toxic Organic Water Contaminants of Phenol and Methylene Blue. J Chem Eng Data 63(3):559–573

21. Leong S, Dan L, Karen H, Wang H, Zhang X (2016) $Ni(OH)_2$ decorated rutile TiO_2 for efficient removal of tetracycline from wastewater. Appl Catal B 198(5):224–233

22. Li H, Li Y, Zhou Y, Li B, Liu D, Liao H (2019) Efficient removal of uranium using a melamine/trimesic acid-modified hydrothermal carbon-based supramolecular organic framework. J Colloid Interface Sci 544:14–24

23. Liu J, Liu G, Liu W (2014) Preparation of water-soluble β-cyclodextrin/poly(acrylic acid)/graphene oxide nanocomposites as new adsorbents to remove cationic dyes from aqueous solutions. Cheml Eng J 257:299–308

24. Liu Z, A C AMAL, A Z AJ, A H, B H (2017) Aqueous tetracycline degradation by coal-based carbon electrocatalytic filtration membrane: Effect of nano antimony-doped tin dioxide coating. Chem Eng J

314:59–68

25. Moussavi G, Hossaini Z, Pourakbar M (2016) High-rate adsorption of acetaminophen from the contaminated water onto double-oxidized graphene oxide. Chem Eng J 287:665–673

26. Pan N, Li L, Ding J, Wang R, Jin Y, Xia C (2017) A Schiff base/quaternary ammonium salt bifunctional graphene oxide as an efficient adsorbent for removal of Th(IV)/U(VI). J Colloid Interface Sci 508:303–312

27. Ponomarev N, Sillanpää M (2019) Combined chemical-templated activation of hydrolytic lignin for producing porous carbon. Ind Crops Prod 135:30–38

28. Salas E, Sun Z, Lu T, Tour A, J M (2010) Reduction of Graphene Oxide via Bacterial Respiration. ACS Nano 4(8):4852–4856

29. Seredych M, Bandosz T (2007) Removal of ammonia by graphite oxide via its intercalation and reactive adsorption. Carbon 45(10):2130–2132

30. Shi X, Qiao Y, An X, Tian Y, Zhou H (2020) High-capacity adsorption of Cr(VI) by lignin-based composite: Characterization, performance and mechanism. Int J Biol Macromol 159:839–849

31. Tan K, Vakili M, Horri B, Poh P, Abdullah A, Salamatinia B (2020) Adsorption of dyes by nanomaterials: Recent developments and adsorption mechanisms. Sep Purif Technol 150:229–242

32. Tejado A, Pena C, Labidi J, Echeverria J, Mondragon I (2007) Physico-chemical characterization of lignins from different sources for use in phenol-formaldehyde resin synthesis. Bioresour Technol 98(8):1655–1663

33. Tian Y, Zhou H (2022) A novel nitrogen-doped porous carbon derived from black liquor for efficient removal of Cr(VI) and tetracycline: Comparison with lignin porous carbon. J Clean Prod 333:130106

34. Wang D, Jian Z, Li G, Yuan J, Li J, Huo Q, Liu Y (2018) A Mesoporous Hexa-Nuclear Copper Cluster-Based MOF with Highly Selective Adsorption of Gas and Organic Dye Molecule. ACS Appl Mater Interfaces 18(11):7114–7121

35. Wang J, Lei S, Liang L (2020) Preparation of porous activated carbon from semi-coke by high temperature activation with KOH for the high-efficiency adsorption of aqueous tetracycline. Appl Sur Sci 530:147187

36. Wang Y, Zhang Y, Hou C, Liu M (2016) Mussel-inspired synthesis of magnetic polydopamine–chitosan nanoparticles as biosorbent for dyes and metals removal. J Taiwan Inst Chem Eng 61:292–298

37. Wu W, Sun Y, Zhou H (2022) In-situ construction of β-Bi_2O_3/Ag_2O photocatalyst from deactivated $AgBiO_3$ for tetracycline degradation under visible light. Chem Eng J 432:134316

38. Xie A, Dai J, Chen X, He J, Chang Z, Yan Y, Li C (2016) Hierarchical porous carbon materials derived from a waste paper towel with ultrafast and ultrahigh performance for adsorption of tetracycline. RSC Adv 6(77):72985–72998

39. Xiong H, Zou D, Zhou D, Dong S, Wang J, Rittmann B (2017) Enhancing degradation and mineralization of tetracycline using intimately coupled photocatalysis and biodegradation (ICPB).

Chem Eng J 316:7–14

40. Yang X, Wang Q, Lai J, Cai Z, Lv J, Chen X, Chen Y, Zheng X, Huang B, Lin G (2020) Nitrogen-doped activated carbons via melamine-assisted NaOH/KOH/urea aqueous system for high performance supercapacitors. Mater Chem Phys 250:123201

41. Yao X, Ji L, Guo J, Ge S, Lu W, Cai L, Wang Y, Song W, Zhang H (2020) Magnetic activated biochar nanocomposites derived from wakame and its application in methylene blue adsorption. Bioresour Technol 302:122842

42. Yu B, Bai Y, Ming Z, Yang H, Chen L, Hu X, Feng S, Yang S (2017) Adsorption behaviors of tetracycline on magnetic graphene oxide sponge. Mater Chem Phys 198:283–290

43. Yu J, Feng H, Tang L, Pang Y, Wang J, Zou J, Xie Q, Liu Y, Feng C, Wang J (2020) Insight into the key factors in fast adsorption of organic pollutants by hierarchical porous biochar. J Hazard Mater 403:123610

44. Zeng H, Qi W, Zhai L, Wang F, Zhang J, Li D (2020) Magnetic biochar synthesized with waterworks sludge and sewage sludge and its potential for methylene blue removal. J Environ Chem Eng 9(5):105951

45. Zhang B, Yang D, Qiu X, Qian Y, Yan M, Li Q (2020) Influences of aggregation behavior of lignin on the microstructure and adsorptive properties of lignin-derived porous carbons by potassium compound activation. J Ind Eng Chem 82:220–227

46. Zhang G, Wo R, Sun Z, Hao G, Liu G, Zhang Y, Guo H, Jiang W (2020) : Effective Magnetic MOFs Adsorbent for the Removal of Bisphenol A, Tetracycline, Congo Red and Methylene Blue Pollutions. Nanomater 11(8)

47. Zhang H, Tian Y, Niu Y, Dong X, Lou H, Zhou H (2022) Lignosulfonate/N-butylaniline hollow microspheres for the removal of Cr(VI): Fabrication, adsorption isotherm and kinetics. J Water Process Eng 46:102588

48. Zhang S, Liao S, Qi F, Liu R, Min Y (2019) Direct deposition of two-dimensional MXene nanosheets on commercially available filter for fast and efficient dye removal. J Hazard Mater 384:121367

49. Zhang S, Wang X, Li J, Wen T, Xu J, Wang X (2014) Efficient removal of a typical dye and Cr(VI) reduction using N-doped magnetic porous carbon. RSC Adv 4(108):63110–63117

50. Zhang W, Yu C, Chang L, Zhong W, Yang W (2018) Three-dimensional nitrogen-doped hierarchical porous carbon derived from cross-linked lignin derivatives for high performance supercapacitors. Electrochim Acta 282:642–652

51. Zhao C, Yin W, Xu J, Zhang Y, Shang D, Guo Z, Wang Q, Wang J, Kong Q (2020) Removal of Tetracycline from Water Using Activated Carbon Derived from the Mixture of Phragmites australis and Waterworks Sludge. ACS Omega 5(26):16045–16052

52. Zhao G, Jiang L, He Y, Li J, Dong H, Wang X, Hu W (2020) Sulfonated graphene for persistent aromatic pollutant management. Adv Mater 23(34):3959–3963

53. Zhao Y, Tian Y, Zhou H, Tian Y (2020) Hydrothermal conversion of black liquor to phenolics and hydrochar: Characterization, application and comparison with lignin. Fuel 280:118651

54. Zhao Y, Zhang H, Zong P, Zhou H, Tian Y (2021) Evaluation of pyrolysis characteristics and product distribution of black liquor using Py-GC/MS and down tube reactor: Comparison with lignin. Fuel 292:120286

55. Zhou H, Shi X, Wu W, An X, Tian Y, Qiao Y (2020) Facile preparation of lignosulfonate/N-methylaniline composite and its application in efficient removal of Cr(VI) from aqueous solutions. Int J Biol Macromol 154:1194–1204

56. Zhu S, Huang X, Ma F, Wang L, Duan X, Wang S (2018) Catalytic Removal of Aqueous Contaminants on N-Doped Graphitic Biochars: Inherent Roles of Adsorption and Nonradical Mechanisms. Environ Sci Technol 52(15):8649–8658

57. Zhu X, Liu Y, Qian F, Zhou C, Zhang S (2014a) Preparation of magnetic porous carbon from waste hydrochar by simultaneous activation and magnetization for tetracycline removal. Bioresour Technol 154(1):209–214

58. Zhu X, Liu Y, Zhou C, Luo G, Zhang S, Chen J (2014b) A novel porous carbon derived from hydrothermal carbon for efficient adsorption of tetracycline. Carbon 77:627–636

Figures

Figure 1

(a-b) SEM micrographs of M-PLAC; (c-h) SEM-EDS images and corresponding elemental mapping images of M-PLAC and (i) the EDS spectrum of M-PLAC.
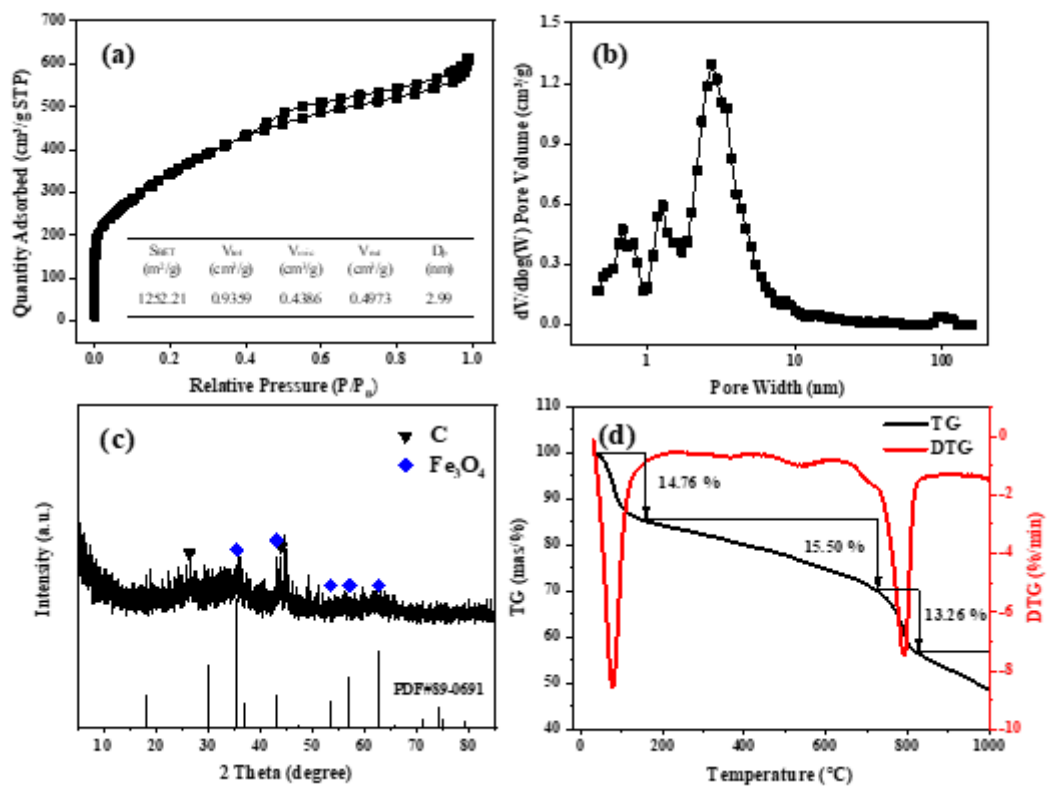
Figure 2

(a) N_2 adsorption-desorption isotherm of M-PLAC; (b) DFT pore size distribution of M-PLAC; (c) XRD pattern of M-PLAC and (d) TG and DTG curves of M-PLAC.
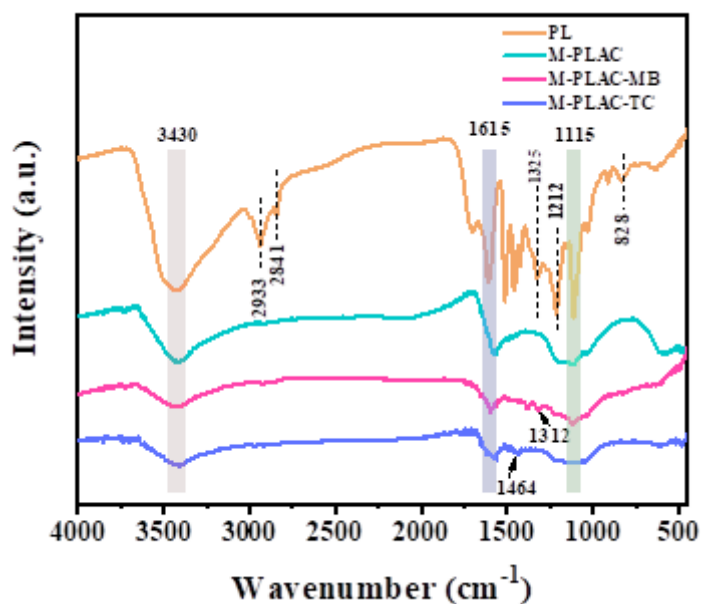

Figure 3

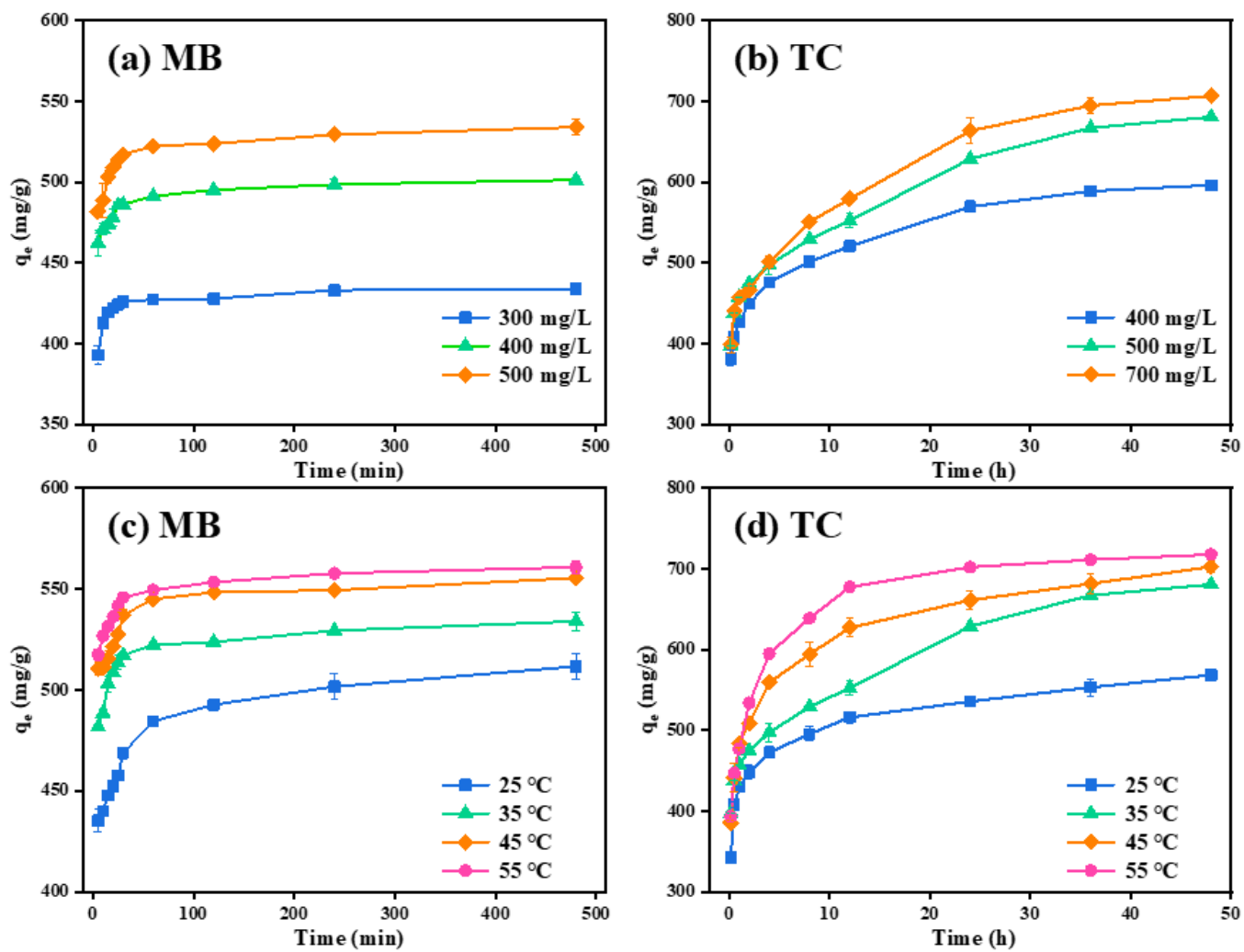FT-IR spectra of PL and M-PLAC before and after adsorption.

Figure 4

Impacts of pollutant concentration, contact time and system temperature on MB ((a) and (c)) and TC ((b) and (d)) adsorption by N-PLAC.
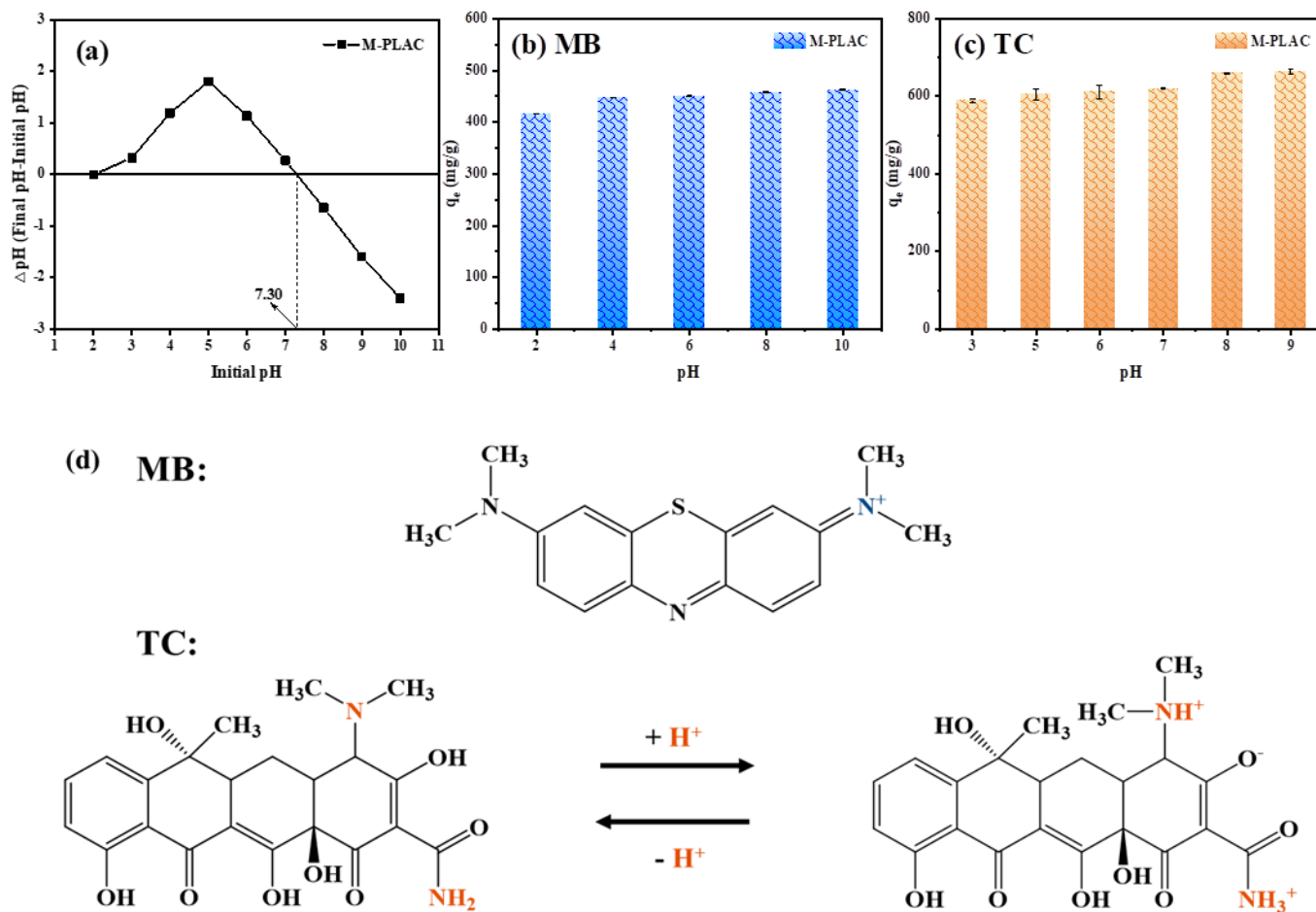
Figure 5

(a) The pH$_{PZC}$ of the M-PLAC; (b) and (c) Influence of initial pH on the adsorption of MB and TC by M-PLAC; (d) Structure of MB and TC.
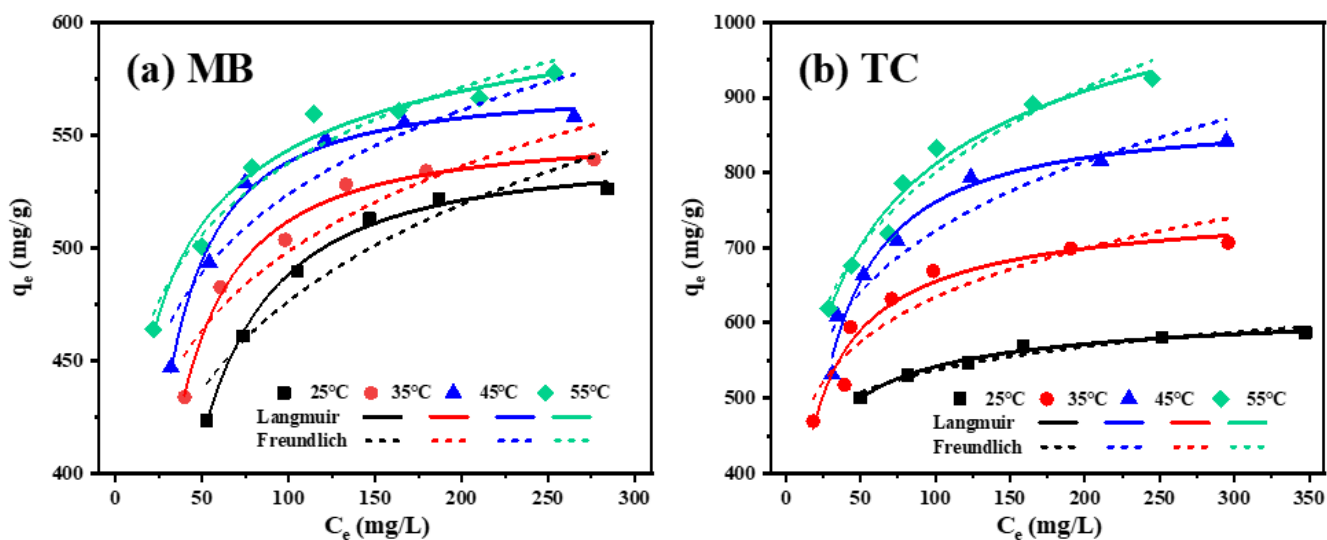
Figure 6

Adsorption isotherm curves of (a) MB and (b) TC adsorption by M-PLAC.
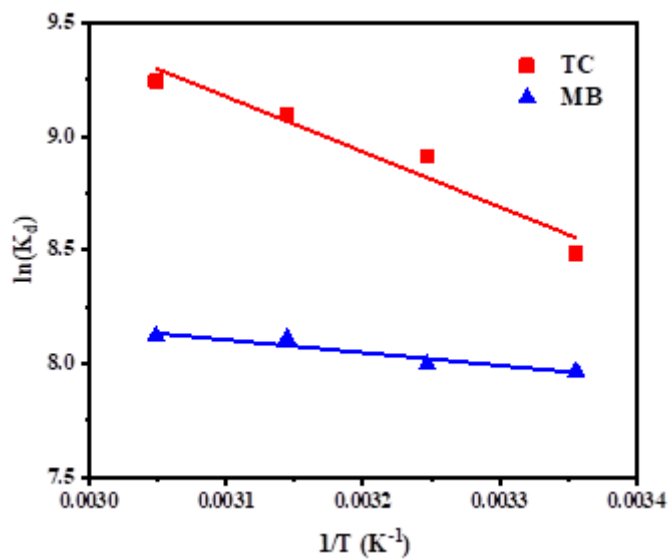
Figure 7

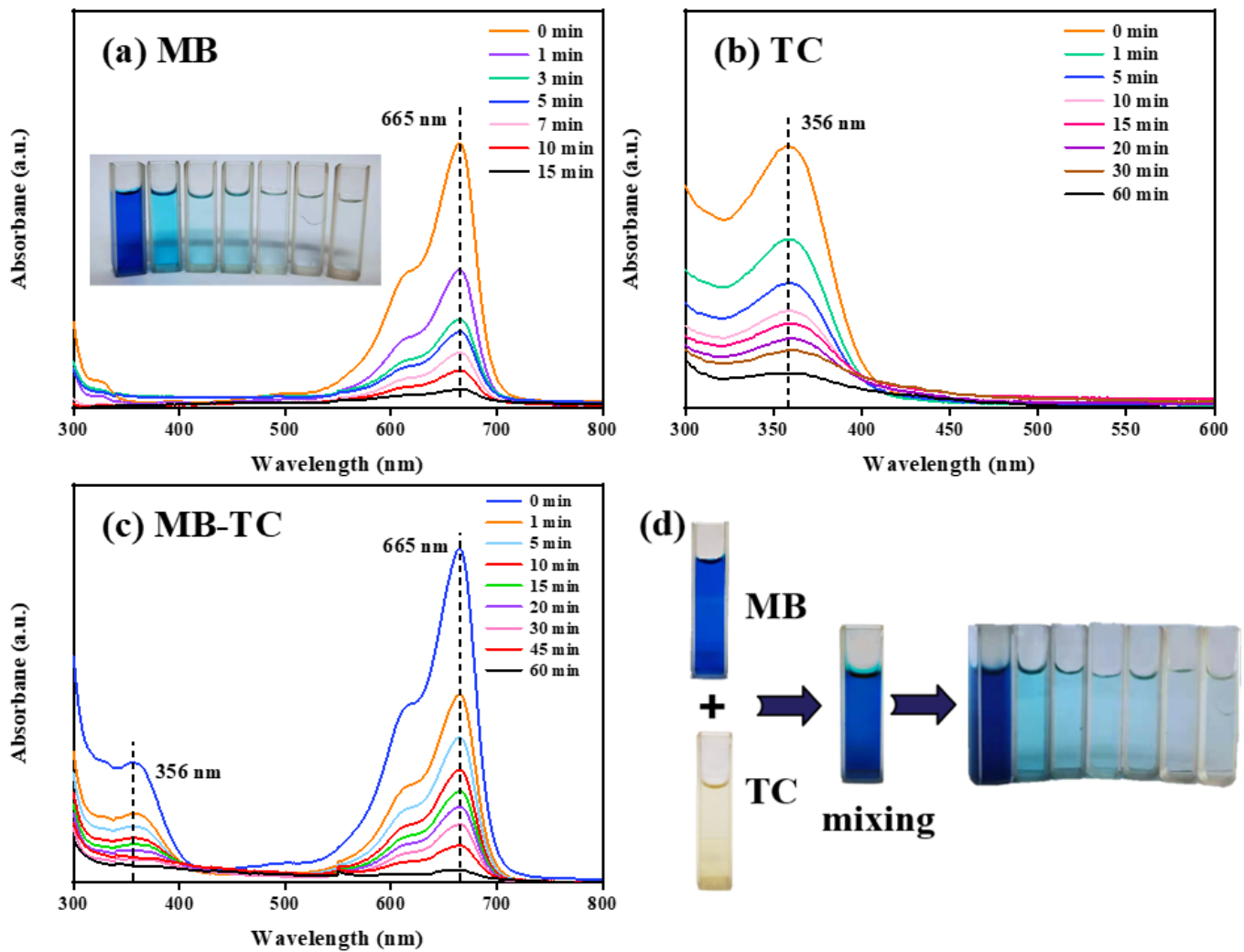The plot of ln(K_d) versus 1/T for the adsorption of MB and TC.

Figure 8

UV-Vis curves and optical images of (a) MB and (b) TC adsorption by M-PLAC; (c) UV-Vis curves of MB/TC binary hybrid solution under different adsorption time; (d) Schematic diagram of selective adsorption of MB/TC binary hybrid solution.
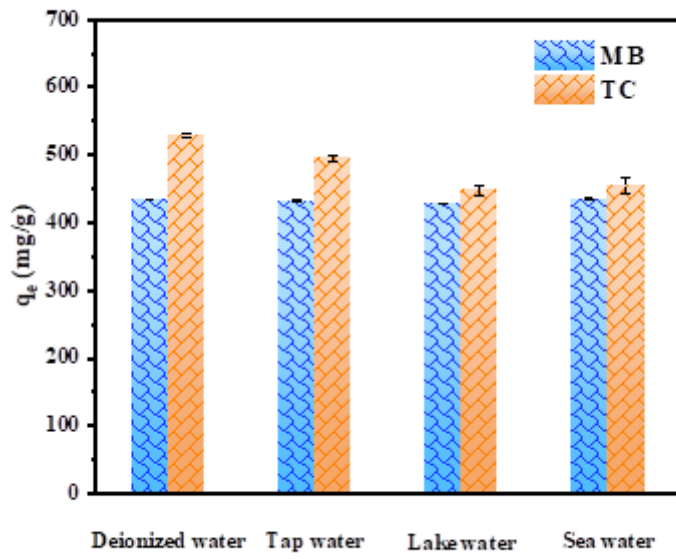
Figure 9

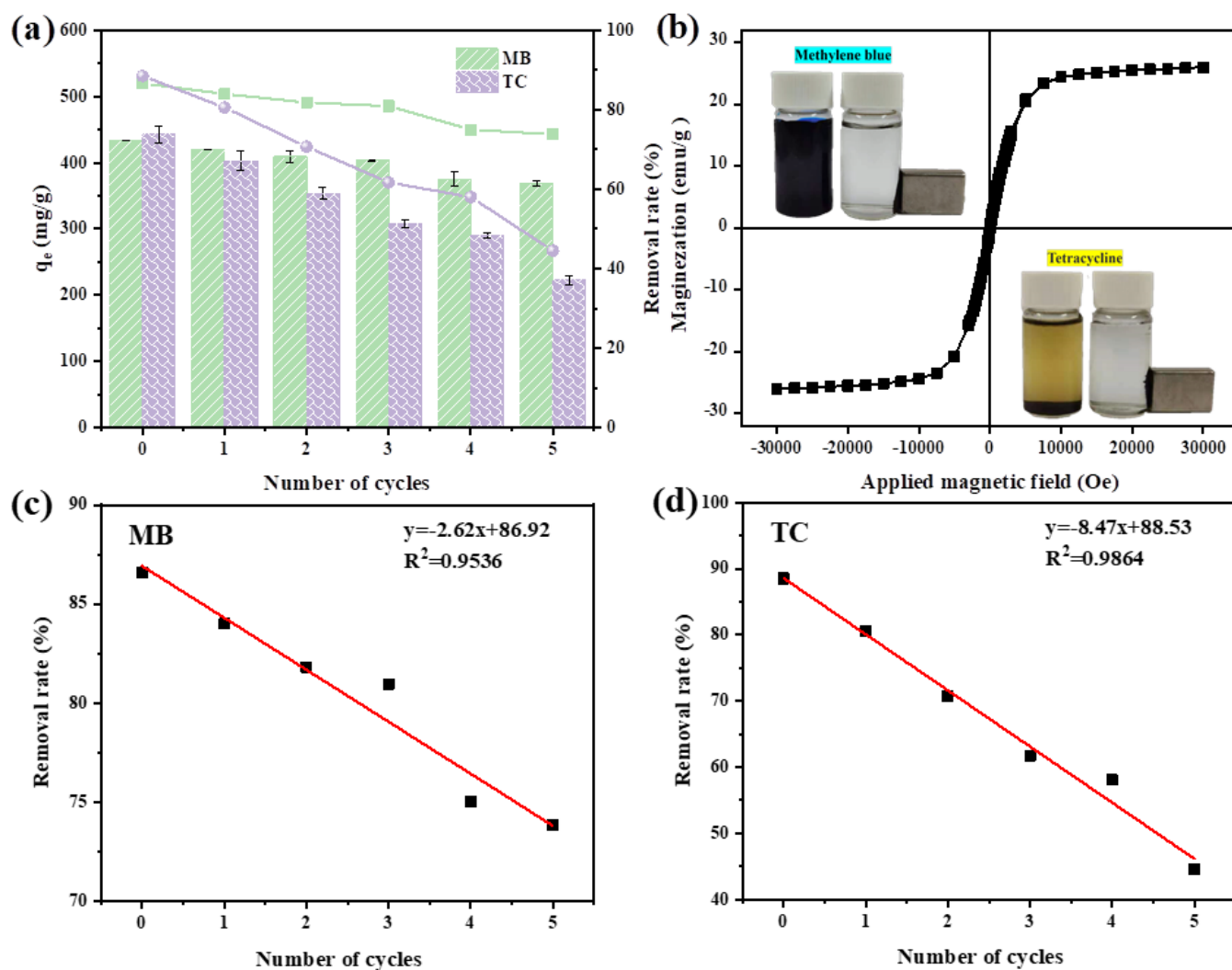The effect of different water quality on MB and TC adsorption by M-PLAC.

Figure 10

(a) Reusability of M-PLAC for MB and TC adsorption; (b) Magnetic hysteresis curve of M-PLAC; (c) The correlation of MB and (d) TC adsorption process with recycles (Insets: the magnetic separation of M-PLAC after MB and TC adsorption).

Supplementary Files

This is a list of supplementary files associated with this preprint. Click to download.

- Scheme1.png
- Scheme2.png
- MPLACSI.docx